



Universiteit  
Leiden

The Netherlands

## **Bridging the gap between physics and chemistry in early stages of star formation**

Nazari, P.

### **Citation**

Nazari, P. (2024, February 13). *Bridging the gap between physics and chemistry in early stages of star formation*. Retrieved from <https://hdl.handle.net/1887/3717029>

Version: Publisher's Version

License: [Licence agreement concerning inclusion of doctoral thesis in the Institutional Repository of the University of Leiden](#)

Downloaded from: <https://hdl.handle.net/1887/3717029>

**Note:** To cite this publication please use the final published version (if applicable).

# Hunt for complex cyanides in protostellar ices with JWST: Tentative detection of $\text{CH}_3\text{CN}$ and $\text{C}_2\text{H}_5\text{CN}$

---

P. Nazari, W. R. M. Rocha, A. E. Rubinstein, K. Slavicinska, M. G. Rachid, E. F. van Dishoeck, S. T. Megeath, R. Gutermuth, H. Tyagi, N. Brunken, M. Narang, P. Manoj, D. M. Watson, N. J. Evans II, S. Federman, J. Muzerolle Page, G. Anglada, H. Beuther, P. Klaassen, L. W. Looney, M. Osorio, T. Stanke, Y.-L. Yang

Accepted for publication in A&A

## Abstract

Nitrogen-bearing complex organic molecules have been commonly detected in the gas phase but not yet in interstellar ices. This has led to the long-standing question of whether these molecules form in the gas phase or in ices. *James Webb* Space Telescope (*JWST*) offers the sensitivity, spectral resolution, and wavelength coverage needed to detect them in ices and investigate whether their abundance ratios are similar in gas and ice. We report the first tentative detection of  $\text{CH}_3\text{CN}$ ,  $\text{C}_2\text{H}_5\text{CN}$ , and the simple molecule,  $\text{N}_2\text{O}$ , based on the CN-stretch band in interstellar ices toward three (HOPS 153, HOPS 370, and IRAS 20126+4104) out of the five protostellar systems observed as part of the Investigating Protostellar Accretion (IPA) GO program with *JWST*-NIRSpec. We also provide upper limits for the two other sources with smaller luminosities in the sample. We detect  $\text{OCN}^-$  in the ices of all sources with typical  $\text{CH}_3\text{CN}/\text{OCN}^-$  ratios of around 1. Ice and gas column density ratios of the nitrogen-bearing species with respect to each other are better matched than those with respect to methanol, which are a factor of  $\sim 5$  larger in the ices than the gas. We attribute the elevated ice column densities with respect to methanol to the difference in snowline locations of nitrogen-bearing molecules and of methanol, biasing the gas-phase observations toward fewer nitrogen-bearing molecules. Moreover, we find tentative evidence for enhancement of  $\text{OCN}^-$ ,  $\text{CH}_3\text{CN}$ , and  $\text{C}_2\text{H}_5\text{CN}$  in warmer ices, although formation of these molecules likely starts along with methanol in the cold prestellar phase. Future surveys combining NIRSpec and MIRI, and additional laboratory spectroscopic measurements of  $\text{C}_2\text{H}_5\text{CN}$  ice, are necessary for robust detection and conclusions on the formation history of complex cyanides.

## 6.1 Introduction

Complex organic molecules (COM; species with  $\geq 6$  atoms containing carbon) are thought to be the precursors of larger species that are necessary for habitable worlds (Herbst & van Dishoeck 2009). COMs have been observed in the gas phase in various stages of star formation such as the prestellar phase (e.g., Bacmann et al. 2012; Jiménez-Serra et al. 2016), protostellar phase (e.g., van Dishoeck et al. 1995b; Cazaux et al. 2003; Jørgensen et al. 2016; Lee et al. 2017; Belloche et al. 2020; van Gelder et al. 2020; Martín-Doménech et al. 2021; Nazari et al. 2021; Diaz-Rodriguez et al. 2022) and even protoplanetary disks (e.g., Öberg et al. 2015; Brunken et al. 2022). These observations have motivated many laboratory and modeling works to understand how and when COMs form (see reviews by Jørgensen et al. 2020; Ceccarelli et al. 2022).

Multiple laboratory studies argue for the formation of these species in icy dust grain mantles in either the translucent phase, cold prestellar phase or during the later warm-up phase around the forming protostar (Öberg et al. 2009b; Meinert et al. 2016; Fedoseev et al. 2017; Muñoz Caro et al. 2019; Qasim et al. 2019a; Chuang et al. 2021; Ioppolo et al. 2021; Santos et al. 2022). If formed in ices, COMs may now be directly detected in protostellar ices with the *James Webb* Space Telescope (*JWST*), while the telescopes preceding *JWST*, such as the *Infrared Space Observatory (ISO)* and the *Spitzer Space Telescope*, did not have the sensitivity, spectral resolution and wavelength coverage (particularly  $\sim 4.4 \mu\text{m}$ ) required to securely detect COMs. Although those telescopes provided valuable information on simple species such as  $\text{H}_2\text{O}$ ,  $\text{CO}_2$ ,  $\text{CH}_4$  and  $\text{NH}_3$ , they could only provide upper limits on most COMs, except for methanol ( $\text{CH}_3\text{OH}$ ) which was detected (Grim et al. 1991; Gerakines et al. 1999; Boogert et al. 2000; Keane et al. 2001; Gibb et al. 2004; Öberg et al. 2008; Pontoppidan et al. 2008; Bottinelli et al. 2010; Öberg et al. 2011; Boogert et al. 2015).

If the icy grains are heated, COMs can sublime into the gas close to the protostar and become observable to telescopes such as the Atacama Large Millimeter/submillimeter Array (ALMA) and the Northern Extended Millimeter Array (NOEMA). Once ices sublime, gas-phase chemistry may occur to either form (larger) COMs from simple species or to alter the abundances of the sublimated COMs (Charnley et al. 1992; Herbst & van Dishoeck 2009; Barone et al. 2015; Balucani et al. 2015; Vazart et al. 2020). Many chemical models have been developed to explain formation of these species on the dust grains or in the gas phase (Garrod et al. 2008; Aikawa et al. 2008; Walsh et al. 2014; Garrod et al. 2022).

Recent ALMA and NOEMA surveys have provided valuable information on the gas-phase column density ratios of COMs in a large number of protostellar systems (e.g., Belloche et al. 2020; Yang et al. 2021; Nazari et al. 2022a; Chen et al. 2023; Taniguchi et al. 2023). These works frequently show that gas-phase nitrogen- and oxygen-bearing COMs have remarkably constant column density ratios across protostellar systems with a large range of mass and luminosity (also see Coletta et al. 2020). These constant ratios are often interpreted as COM formation in similar environments, likely in the prestellar ices. However, the cold, hard evidence is to directly detect COMs in ices and compare the ice and gas

abundances to search for any relation between the two.

With the launch of *JWST*, COMs in ices can be studied with the spectroscopic instruments; Mid-InfraRed Instrument (MIRI) and Near InfraRed Spectrograph (NIRSpec). Already, hints for oxygen-bearing COMs are observed in MIRI studies (Yang et al. 2022; Rocha et al. 2023) building on the *ISO* and *Spitzer* results (Schutte et al. 1999; Öberg et al. 2011). Nitrogen-bearing COMs are as important, in particular, because nitrogen contributes to forming amino acids and nucleobases required to develop habitable worlds. Yet, elemental nitrogen is a factor of  $\sim 5$  less abundant than oxygen, making it more difficult to observe N-bearing molecules. Therefore, much less is known about the formation and evolution of N-bearing COMs in ices or in the gas. In fact, the only N-bearing COM considered in interstellar ices with *JWST* is formamide ( $\text{NH}_2\text{CHO}$ ) where Slavicinska et al. (2023) used the Early Release Science program, Ice Age (McClure et al. 2023) and the guaranteed time observation program, JOYS (van Dishoeck et al. 2023) to hunt for formamide at  $7.24 \mu\text{m}$ , which was suggested previously to be in protostellar ices by Schutte et al. (1999). Even then, Slavicinska et al. (2023) could find only upper limits on formamide column density. In this paper we use *JWST*-NIRSpec to search for nitrogen-bearing COMs through their strong CN stretching band and provide the first tentative detection of N-bearing COMs in ices.

We focus on methyl cyanide ( $\text{CH}_3\text{CN}$ ) and ethyl cyanide ( $\text{C}_2\text{H}_5\text{CN}$ ). They have a strong vibrational transition in the  $\sim 4.4 - 4.7 \mu\text{m}$  range. Although methyl cyanide is one of the most used tracers of the hot core phase, its formation mechanism has been debated for decades (Huntress & Mitchell 1979; Wilner et al. 1994; Walsh et al. 2014; Le Gal et al. 2019; Nazari et al. 2023c). Moreover, it is the most abundant nitrogen-bearing COM in the gas-phase (e.g., Calcutt et al. 2018b; Yang et al. 2021). Therefore, if the bulk of  $\text{CH}_3\text{CN}$  were to form in ices, it is one of the few nitrogen-bearing species that could be observed by *JWST* providing important clues to its formation mechanism. Previously, Rachid et al. (2022) investigated the presence of  $\text{CH}_3\text{CN}$  in *ISO* (also see Gibb et al. 2004) and *Spitzer* spectra and found upper limits on its ice column densities. We also include  $\text{C}_2\text{H}_5\text{CN}$  in our work given that it has a transition right next to  $\text{CH}_3\text{CN}$ , so it is impossible to quantify one without the other. Furthermore, the chemistry of  $\text{C}_2\text{H}_5\text{CN}$  is thought to be related to  $\text{CH}_3\text{CN}$  (Bulak et al. 2021), and it has high gas-phase abundances with  $\text{C}_2\text{H}_5\text{CN}/\text{CH}_3\text{CN} \sim 0.1$  (Nazari et al. 2022a). The hunt for  $\text{CH}_3\text{CN}$  and  $\text{C}_2\text{H}_5\text{CN}$  is now facilitated by the recent laboratory studies on their spectroscopy (Moore et al. 2010; Rachid et al. 2022).

In addition, we use the column density of  $\text{OCN}^-$  ( $\sim 4.6 \mu\text{m}$ ; van Broekhuizen et al. 2005) in ices as a reference species. Given that  $\text{OCN}^-$  is thought to form from  $\text{HNCO}$  (a molecule observed abundantly in the gas phase) and  $\text{NH}_3$  in ices (Schutte et al. 1999; Novozamsky et al. 2001; Schutte & Khanna 2003; Ruaud et al. 2016),  $\text{OCN}^-$  is an ideal reference for nitrogen-bearing molecules. When ices sublimate close to the protostar,  $\text{OCN}^-$  is thought to turn back into  $\text{HNCO}$  as it sublimates into the gas (Öberg et al. 2009a). Therefore, we compare the ice column density ratios with respect to  $\text{OCN}^-$  with the gas column density ratios with respect to  $\text{HNCO}$ .

In this work we search for  $\text{CH}_3\text{CN}$  and  $\text{C}_2\text{H}_5\text{CN}$  around the protostars observed

by *JWST* as part of the Investigating Protostellar Accretion (IPA; Federman et al. 2023; Narang et al. 2023) program and tentatively detect them around three protostars for the first time. We first fit a local continuum to these data, fit laboratory data to the spectra and measure the  $\text{CH}_3\text{CN}$ ,  $\text{C}_2\text{H}_5\text{CN}$  and  $\text{OCN}^-$  ice column densities (Sect. 6.4). We then compare our column density ratios with the gas-phase ratios in Sect. 6.5, discuss the chemical interpretations of our findings in Sect. 6.6 and conclude in Sect. 6.7.

## 6.2 Observations and methods

### 6.2.1 Data

Here we study the five protostars observed by *JWST* NIRSpec (Bagnasco et al. 2007; Jakobsen et al. 2022; Böker et al. 2023) in the Integral Field Spectroscopy mode (IFU; Böker et al. 2022) as part of the IPA program (project ID: 1802, PI: T. Megeath). The protostellar systems observed by this program have a range of bolometric luminosities ( $\sim 0.2 - 10^4 L_\odot$ ) and protostellar masses ( $\sim 0.12 - 12 M_\odot$ ). They are, in order of increasing luminosity, IRAS 16253-2429 (hereafter IRAS 16253), B335-IRS (hereafter B335), HOPS 153, HOPS 370, and IRAS 20126+4104 (hereafter IRAS 20126). Table 6.A.1 presents the bolometric luminosities and distances of the objects. Data reduction is explained in detail in Federman et al. (2023) and Narang et al. (2023); thus we give only a brief overview of the data. The objects were observed in the G395M setting (spectral resolving power  $R$  of  $\sim 1000$ ) with a 4-point dither pattern, a spatial coverage of  $\sim 6'' \times 6''$ , and a spatial resolution of  $\sim 0.2''$ . The observations cover the wavelength range between  $\sim 2.87 \mu\text{m}$  and  $\sim 5.27 \mu\text{m}$ . This paper focuses on the wavelength range of  $\sim 4.4 - 4.7 \mu\text{m}$ , as complex and simple species with a CN bond such as  $\text{CH}_3\text{CN}$ ,  $\text{C}_2\text{H}_5\text{CN}$ , HCN,  $\text{HC}_3\text{N}$ , and  $\text{OCN}^-$  are all known to have one of their strongest transitions (the CN stretch) around this region (Soifer et al. 1979; Russo & Khanna 1996; Gibb et al. 2000; Moore et al. 2010; Rachid et al. 2022).

This work focuses on the ice features that are absorbed in the continuum, but the wavelength range of interest is also where CO rotational-vibrational gas-phase emission lines are known to lie which make the analysis of the ices more difficult (Federman et al. 2023; Rubinstein et al. 2023). Therefore, we avoided these emission lines in two ways. First, we searched the data cubes for the best spatial regions at which these gas-phase lines are less prominent. For each source we extracted the spectrum from such a region where CO emission lines are either not observed or are relatively weak. However, due to the potential remaining uncertainty by the residual gas-phase CO lines, we also analyzed the spectra extracted from the same positions using the emission-line subtracted cubes produced by Rubinstein et al. (2023). This method provided two sets of spectra with either no gas-phase emission lines or relatively weak ones which facilitated the identification of the CN stretching band.

In all cases the spectra were extracted off-source with their centers given in Table 6.A.1 (also see Fig. 6.A.1). The radius of the aperture ( $0.6''$ ) is taken as  $\sim 3$  times the full width at half maximum (FWHM) of the point spread function of

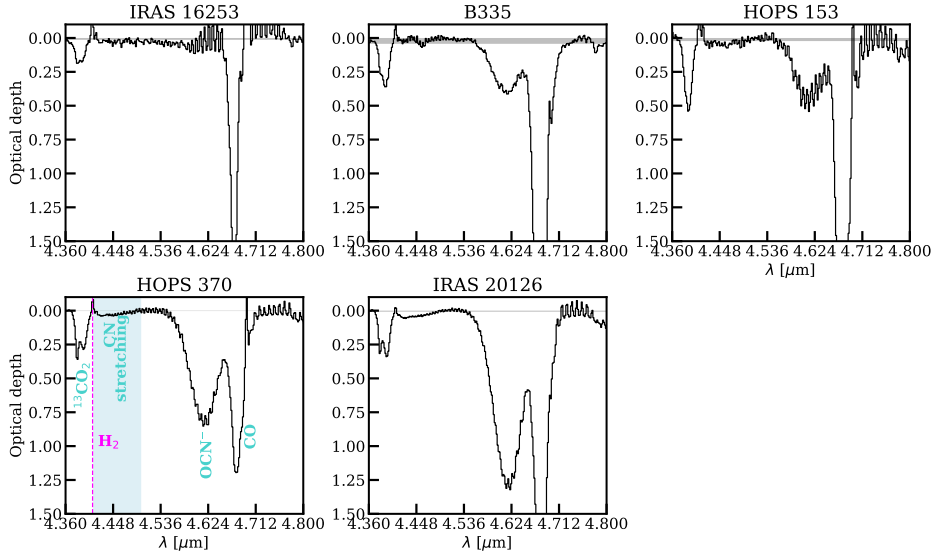


**Figure 6.1:** Calculated optical depth for all 5 sources in the wavelength range of interest. Gray shaded area shows the optical depth  $3\sigma$  uncertainty level. Although the spectra are extracted off source (see table 6.A.1), some CO emission lines are still seen in the spectra. The CN stretching mode vibration band is shaded with light blue. The emission line between the  $^{13}\text{CO}_2$  ice feature and the CN stretching band is the  $\text{H}_2$  0–0 S(10) line (marked with the dashed magenta line).

NIRSpec-IFU at  $4.9\ \mu\text{m}$ . The rms on the continuum optical depth was calculated using the error plane of each data cube by selecting two spectral regions with least (or no) spectral features. The  $\sigma$  on optical depth ranges from  $\sim 0.001$  to  $\sim 0.01$  (see Table 6.A.1).

### 6.2.2 Continuum determination and subtraction

The continuum was fitted locally and subsequently subtracted using the polynomial function method included in the ENIGMA fitting tool (Rocha et al. 2021) to isolate the bands of interest from the broad water combination mode at  $\sim 4.45\ \mu\text{m}$ . This continuum identification method has been commonly used in the literature for ice analysis (e.g., Öberg et al. 2011; Boogert et al. 2022; Slavicinska et al. 2023). Figure 6.A.2 presents the continuum fitted to the data. We note that grain shape effects are not expected to dominate and change the ice features in our region of interest (e.g., Palumbo et al. 1995; Dartois et al. 2022). The continuum subtracted fluxes ( $F_\lambda$ ) were then converted to optical depth through  $-\ln(F_\lambda^{\text{data}}/F_\lambda^{\text{cont}})$ . Figure 6.1 presents the continuum-subtracted spectra converted into the optical depth scale for the five sources. The  $3\sigma$  on optical depth is highlighted on Fig. 6.1; it is larger for the lower luminosity sources.

The three most luminous sources (HOPS 153, HOPS 370, and IRAS 20126)

show a significant ( $S/N \gtrsim 3$ ) absorption feature at  $4.44 \mu\text{m}$ . Continuum identification for IRAS 16253 is uncertain due to the remaining CO emission lines, hence the significance of the absorption feature at  $4.44 \mu\text{m}$  is unclear. For B335 the absorption feature is at around the  $3\sigma$  level but because of the residual CO emission lines, it is difficult to conclude. Using the emission subtracted spectra the absorption feature of B335 is less than the  $3\sigma$  level and thus is not significant. Hence, we focus our analysis only on the three most luminous sources.

## 6.3 Band identification and fitting

### 6.3.1 $\text{CH}_3\text{CN}$

Figure 6.2 presents a blow-up of the  $4.35\text{--}4.5 \mu\text{m}$  range for IRAS 20126, which includes the the  $^{13}\text{CO}_2$  ice feature at  $\leq 4.40 \mu\text{m}$  and the CN-bearing species absorption feature at the longer wavelengths ( $4.4 - 4.5 \mu\text{m}$ ). Rachid et al. (2022) considered  $\text{CH}_3\text{CN}$  infrared spectra in seven different ice mixtures and various temperatures (15–140 K). The line profiles of these various mixtures peak between  $4.410 \mu\text{m}$  up to  $4.442 \mu\text{m}$ . The left panel of Fig. 6.2 presents two of the  $\text{CH}_3\text{CN}$  ice mixture spectra from Rachid et al. (2022) that have the shortest and longest peak wavelengths as well as a large FWHM. Figure 6.2 shows that although  $\text{CH}_3\text{CN}$  could be responsible for the absorption feature at  $4.4 - 4.45 \mu\text{m}$ , the entire feature up to  $4.5 \mu\text{m}$  is too wide to be explained by  $\text{CH}_3\text{CN}$  mixtures alone, thus Sect. 6.3.2 explores other species that could be responsible for the rest of the absorption feature.

We opted for fitting the  $\sim 4.40 - 4.45 \mu\text{m}$  region with a minimum number of  $\text{CH}_3\text{CN}$  ice mixtures. We used Fig. 3 (FWHM versus peak position) and Table B.2 of Rachid et al. (2022) to carefully determine the ice mixtures that best fit the data. The minimum number of components requires features with large FWHM. The mixtures from Rachid et al. (2022) that match the absorption band at  $\lambda > 4.4 \mu\text{m}$  in peak position and have relatively large FWHM ( $\sim 8 - 15 \text{cm}^{-1}$ ) are  $\text{CH}_3\text{CN}:\text{CO}_2$ ,  $\text{CH}_3\text{CN}:\text{NH}_3$ ,  $\text{CH}_3\text{CN}:\text{CO}$  (at higher temperatures) and mixtures with water. From these mixtures, those with water (polar ices) have the largest FWHM, and from those, the mixture  $\text{CH}_3\text{CN}:\text{H}_2\text{O}:\text{CO}_2$  is favored to  $\text{CH}_3\text{CN}:\text{H}_2\text{O}$  and  $\text{CH}_3\text{CN}:\text{H}_2\text{O}:\text{CH}_4:\text{NH}_3$  because it peaks at longer wavelengths. Although favored, the mixture of  $\text{CH}_3\text{CN}:\text{H}_2\text{O}:\text{CO}_2$  cannot fit the entire absorption feature thus, at least one additional component is needed to fit the  $\sim 4.40 - 4.45 \mu\text{m}$  feature.

We chose the apolar mixture  $\text{CH}_3\text{CN}:\text{CO}$  as this additional component. Compared to  $\text{CH}_3\text{CN}:\text{CO}_2$ ,  $\text{CH}_3\text{CN}:\text{CO}$  at high temperatures peaks at longer wavelengths, so it better matches the data. Between the mixtures with CO or  $\text{NH}_3$  we opted for  $\text{CH}_3\text{CN}:\text{CO}$  for two reasons: (i) the mixture with CO has a shoulder at shorter wavelengths ( $\sim 4.41 \mu\text{m}$ , see right panel of Fig. 6.2) that avoids adding unnecessary additional components, and (ii) the CO mixture is likely more relevant for interstellar ices (Boogert et al. 2015). With  $\text{CH}_3\text{CN}:\text{H}_2\text{O}:\text{CO}_2$  and  $\text{CH}_3\text{CN}:\text{CO}$  the main absorption feature can be reasonably fitted, but we included the  $\text{CH}_3\text{CN}:\text{CO}_2$  mixture to avoid having a dip in between the peak of

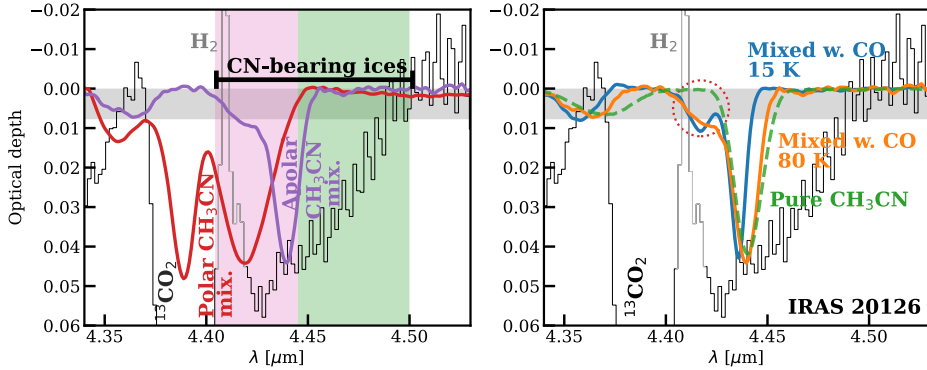


**Figure 6.2:** Continuum subtracted spectrum of IRAS 20126 in the  $4.35 - 4.5 \mu\text{m}$  range. The shaded gray area shows the  $3\sigma$  uncertainty on optical depth. The  $\text{H}_2$  emission line at  $\sim 4.41 \mu\text{m}$  is shown in gray. *Left:* Two of the most extreme  $\text{CH}_3\text{CN}$  ice mixtures in peak position with large FWHM from Rachid et al. (2022) are shown in red and purple to demonstrate that the shaded green region cannot be explained by  $\text{CH}_3\text{CN}$  mixtures but the shaded pink region can. Red is the  $\text{CH}_3\text{CN}:\text{H}_2\text{O}:\text{CO}_2$  (1:5:2, 50 K) mixture and purple is the  $\text{CH}_3\text{CN}:\text{CO}$  (1:10, 80 K). *Right:* mixtures of  $\text{CH}_3\text{CN}:\text{CO}$  (1:10) at 15 K (blue) and 80 K (orange) to demonstrate that the one at 80 K has a larger FWHM and peak position. In addition, the red circle shows the shoulder that does not exist in the pure  $\text{CH}_3\text{CN}$  (dashed green) laboratory spectra of Rachid et al. (2022) and is produced in the  $\text{CH}_3\text{CN}$  ice feature when mixed with CO.

$\text{CH}_3\text{CN}:\text{H}_2\text{O}:\text{CO}_2$  and  $\text{CH}_3\text{CN}:\text{CO}$ . Given the present uncertainties it is not possible to argue whether  $\text{CH}_3\text{CN}:\text{CO}_2$  is strictly necessary to fit the absorption feature. We emphasize that our final fits (Fig. 6.3) are not unique and a fit can also be obtained by for example increasing the  $\text{CH}_3\text{CN}:\text{CO}_2$  component and decreasing the  $\text{CH}_3\text{CN}:\text{H}_2\text{O}:\text{CO}_2$  component. However the final column density of  $\text{CH}_3\text{CN}$  will only be affected by less than a factor of  $\sim 2$ .

It is not possible to constrain the temperature of the ice for  $\text{CH}_3\text{CN}:\text{CO}_2$  and  $\text{CH}_3\text{CN}:\text{H}_2\text{O}:\text{CO}_2$  mixtures apart from arguing that they should be below  $\sim 50$  K and  $\sim 120$  K under laboratory conditions, respectively, to retain the large FWHM. However, for the  $\text{CH}_3\text{CN}:\text{CO}$  mixture, high temperatures ( $\sim 80$  K as opposed to  $\sim 15$  K) better match the data by producing a larger FWHM and being centered at longer wavelengths (see right panel of Fig. 6.2). We note that  $\sim 80$  K in the laboratory conditions is  $\sim 30$  K in interstellar conditions (e.g., Boogert et al. 2015). This implies that the temperatures of ice mixtures under laboratory conditions are not equivalent to the true ice temperature in the protostellar environments because of the different time scales in those two conditions. In terms of ice morphology, this means that phase transitions and structural changes (e.g., amorphous to crystalline), would happen at higher temperatures in the laboratory. Thus, the 80 K ice mixture of  $\text{CH}_3\text{CN}$  and CO in the laboratory which still includes CO trapped in the ice is similar to a 30 K ice mixture of  $\text{CH}_3\text{CN}$  and CO in protostellar environments with most CO likely sublimated, but some trapped in the ice. This

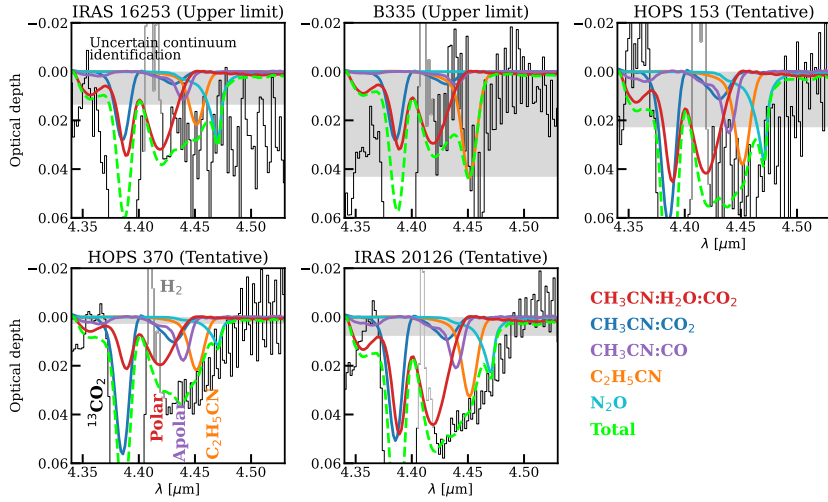


**Figure 6.3:** Fitted  $\text{CH}_3\text{CN}$ ,  $\text{C}_2\text{H}_5\text{CN}$  and  $\text{N}_2\text{O}$  models on top of the continuum subtracted data (black). The models of the various mixtures of the ice are color coded as follows,  $\text{CH}_3\text{CN}:\text{H}_2\text{O}:\text{CO}_2$  (1:5:2, 50 K, red),  $\text{CH}_3\text{CN}:\text{CO}_2$  (1:10, 15 K, blue),  $\text{CH}_3\text{CN}:\text{CO}$  (1:10, 80 K, purple),  $\text{C}_2\text{H}_5\text{CN}$  (orange, 50 K), and  $\text{N}_2\text{O}$  (70 K, cyan). The total fit is shown with the dashed green line. The  $3\sigma$  uncertainty on optical depth is shown in shaded gray. Continuum identification of IRAS 16253 is uncertain and thus the significance of the observed feature is unclear. The  $\text{H}_2$  emission line is shown in gray and ignored when fitting (see also Fig. 6.A.3).

trapping can be seen from the effect of CO on the  $\text{CH}_3\text{CN}$  absorption feature at  $\sim 4.41 \mu\text{m}$  (see the difference between  $\text{CH}_3\text{CN}:\text{CO}$  mixture and pure  $\text{CH}_3\text{CN}$  in right panel of Fig. 6.2).

### 6.3.2 $\text{C}_2\text{H}_5\text{CN}$ and $\text{N}_2\text{O}$

There is considerable absorption (at  $\gtrsim 3\sigma$ ) in the  $4.442 < \lambda < 4.5 \mu\text{m}$  region of IRAS 20126 (see left panel of Fig. 6.2). Therefore, we searched the literature for other simple and complex molecules with absorption bands in this region. In total we searched for  $\sim 30$  pure ices or ice mixtures at various temperatures ( $\sim 10$ – $150$  K) to examine potential contribution from those in the  $\sim 4.4$ – $4.52 \mu\text{m}$  region. We particularly used NASA’s Optical Constants database<sup>1</sup>, the Cosmic Ice Laboratory database<sup>2</sup> and the Leiden Ice Database for Astrochemistry (Rocha et al. 2022). This search included Oxygen-bearing species such as  $\text{CH}_3\text{OCH}_3$ ,  $\text{CH}_3\text{CHO}$  and CO in addition to many nitrogen-bearing species such as  $\text{HNCO}$  and  $\text{N}_2\text{O}$ , and in particular those with a CN bond,  $\text{C}_2\text{H}_5\text{CN}$ ,  $\text{C}_2\text{H}_3\text{CN}$ ,  $\text{C}_2\text{N}_2$ , and  $\text{HC}_n\text{N}$ . Among the considered species,  $\text{C}_2\text{H}_5\text{CN}$  and  $\text{N}_2\text{O}$  in addition to  $\text{CH}_3\text{CN}$  were found to best match the absorption feature observed at  $\sim 4.4$ – $4.52 \mu\text{m}$ . The other species

<sup>1</sup><https://ocdb.smce.nasa.gov/search/ice?t=gw9anjm2av>

<sup>2</sup><https://science.gsfc.nasa.gov/691/cosmicice/constants.html>

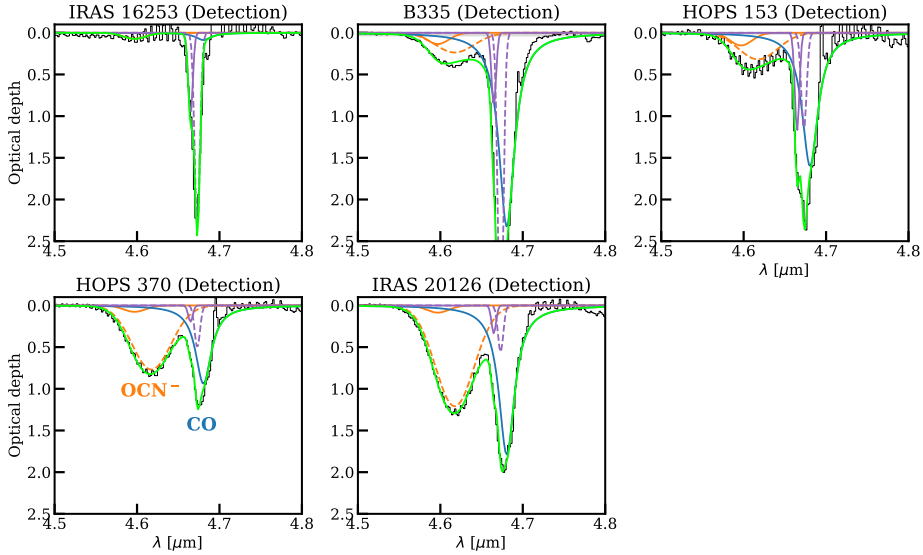


**Figure 6.4:** Fitted model to  $\text{OCN}^-$  absorption feature. Orange dashed and solid lines show the red and blue  $\text{OCN}^-$  (sometimes attributed to CO absorption instead), showing that the bulk of the XCN feature is dominated by  $\text{OCN}^-$ . The blue and purple lines show the Lorentzian and Gaussian contributions to the CO band, respectively. The XCN and CO bands are fitted simultaneously. The total fit is shown in green. The  $3\sigma$  uncertainty on optical depth is shown in shaded gray. The y-axis limit is set for better visibility of the ice features in all sources which cuts off the fit to the CO band in B335. The fit to the CO ice band in B335 is similar to the other sources and does not over predict the data.

did not match the data because either their peak did not match or if they had an absorption feature at the right wavelength, they showed a stronger one at a wavelength with no absorption feature in the spectrum (e.g., HCN).

To the best of our knowledge, there is no laboratory study of ethyl cyanide or  $\text{N}_2\text{O}$  ice mixtures at infrared wavelengths. Therefore, we took the pure amorphous and crystalline absorbance spectrum of  $\text{N}_2\text{O}$  at 10 K and 70 K from Gerakines & Hudson (2020). The 70 K spectrum better fit the data because its peak is at shorter wavelengths. Moreover, we took the imaginary refractive indices ( $k_\nu$ ) of pure laboratory measurements of amorphous  $\text{C}_2\text{H}_5\text{CN}$  at various temperatures (50–110 K) from Moore et al. (2010). Before fitting the observed spectra we converted  $k_\nu$  from Moore et al. (2010) to optical depth using

$$\tau = 4\pi k_\nu \nu d, \quad (6.1)$$

where  $\nu$  is the wavenumber and  $d$  is the ice thickness of  $2.29 \mu\text{m}$  from the experiments of Moore et al. (2010). This is a first order approximation because we do not have the information on the Fresnel coefficients for these measurements.

Figure 6.3 presents our final model fits to the  $4.4 - 4.52 \mu\text{m}$  band and the

decomposition of that model into components for the five objects. We also fitted the spectra with gas-phase emission lines subtracted and the final models for those are shown in Fig. 6.A.3. Using either the spectra before or after subtraction of emission lines we obtain only upper limits on CH<sub>3</sub>CN and C<sub>2</sub>H<sub>5</sub>CN toward IRAS 16253 (due to the uncertain continuum identification) and B335. However, using both versions of the spectra we tentatively detect CH<sub>3</sub>CN, C<sub>2</sub>H<sub>5</sub>CN, and N<sub>2</sub>O toward the other three sources, all for the first time in interstellar ices.

### 6.3.3 OCN<sup>-</sup>

The absorption feature at 4.61 μm is often referred to as the ‘XCN’ band and is extensively studied (Gibb et al. 2004; van Broekhuizen et al. 2005; Fraser et al. 2005; Öberg et al. 2011; Maté et al. 2012; Boogert et al. 2022). This band was suggested by van Broekhuizen et al. (2005) to be composed of two Gaussian profiles (at 2165.7 cm<sup>-1</sup> with FWHM of 26 cm<sup>-1</sup> and at 2175.4 cm<sup>-1</sup> with FWHM of 15 cm<sup>-1</sup>). One (2165.7 cm<sup>-1</sup>) can be attributed to OCN<sup>-</sup> and the other one has been attributed to either CO bonding to grain surfaces or OCN<sup>-</sup> in apolar ice environments (Fraser et al. 2005; Öberg et al. 2011). Moreover, the XCN band is blended with the stretching mode of CO which will affect the fitting of this region. The CO band is proposed to be composed of a Lorentzian profile (peak at 2136.5 cm<sup>-1</sup> with FWHM 10.6 cm<sup>-1</sup>) and two Gaussian profiles (peaks at 2139.9 cm<sup>-1</sup> and 2143.7 cm<sup>-1</sup> with FWHM of 3.5 cm<sup>-1</sup> and 3.0 cm<sup>-1</sup>) by Pontoppidan et al. (2003). Therefore, we use these line profiles in addition to the two Gaussian profiles suggested for the XCN band by van Broekhuizen et al. (2005) to fit the feature between 4.56 μm and 4.7 μm simultaneously. This method has also been used in Boogert et al. (2022) for several high-mass protostars. The fits, which match the data very well, are shown in Fig. 6.4.

## 6.4 Column densities

### 6.4.1 CH<sub>3</sub>CN and C<sub>2</sub>H<sub>5</sub>CN

Column densities for CH<sub>3</sub>CN and C<sub>2</sub>H<sub>5</sub>CN are calculated using,

$$N = \int \tau d\nu / A, \quad (6.2)$$

where  $A$  is the band strength,  $\tau$  is the optical depth and the integral is performed in the wave number space. The measured ice column densities or upper limits are given in Table 6.1. The band strengths ( $A$ ) used for determination of ice column densities are given in Table 6.A.2. The band strengths for the CH<sub>3</sub>CN ice mixtures are taken from Rachid et al. (2022) as 0.8, 0.8, and 1.75 times the band strength of pure CH<sub>3</sub>CN ( $1.9 \times 10^{-18}$  cm molecule<sup>-1</sup>) for CH<sub>3</sub>CN:CO<sub>2</sub>, CH<sub>3</sub>CN:CO and CH<sub>3</sub>CN:H<sub>2</sub>O:CO<sub>2</sub>, respectively. The band strength for C<sub>2</sub>H<sub>5</sub>CN (50 K) is calculated as  $2.86 \times 10^{-18}$  cm molecule<sup>-1</sup> using the following equation (e.g., Roser et al. 2021)

**Table 6.1:** Ice column densities

Sources	$N_{\text{CH}_3\text{CN}}$ ( $\text{cm}^{-2}$ )	$N_{\text{C}_2\text{H}_5\text{CN}}$ ( $\text{cm}^{-2}$ )	$N_{\text{OCN}^-}$ ( $\text{cm}^{-2}$ )
IRAS 16253	$<2.5 \times 10^{17}$	$<7.1 \times 10^{16}$	$2.6 \times 10^{16}$
B335	$<2.0 \times 10^{17}$	$<1.4 \times 10^{17}$	$5.0 \times 10^{16}$
HOPS 153	$4.3 \times 10^{17}$	$1.2 \times 10^{17}$	$6.8 \times 10^{16}$
HOPS 370	$2.8 \times 10^{17}$	$7.1 \times 10^{16}$	$1.6 \times 10^{17}$
IRAS 20126	$4.0 \times 10^{17}$	$1.1 \times 10^{17}$	$2.6 \times 10^{17}$

**Notes.** The uncertainties are estimated at around 30% for  $\text{OCN}^-$  and at around 50% for the other two species.

$$A = \frac{m}{\rho N_A} \int 4\pi\nu k_\nu d\nu, \quad (6.3)$$

where  $m$  is the molar mass of ethyl cyanide ( $55.08 \text{ g mol}^{-1}$ ),  $\rho$  is its ice density ( $0.703 \text{ g cm}^{-3}$ ; Gerakines et al. 2022), and  $N_A$  is the Avogadro's number. The band strength of  $\text{C}_2\text{H}_5\text{CN}$  is also determined in Gerakines et al. (2022) based on the results of Moore et al. (2010) as  $2.8 \times 10^{-18} \text{ cm molecule}^{-1}$  which agrees well with what is found here. For the upper limits we take the maximum of the measured upper limit from the spectra before (Fig. 6.3) and after the emission line subtraction (Fig. 6.A.3). The uncertainties on column densities for the tentative detections are dominated by the error in continuum fitting and the error on band strengths. The uncertainties on the band strengths are normally on the order of  $\sim 30\%$  and those based on the choice of the continuum and the line blending are estimated as  $\sim 40\%$ , resulting in a total uncertainty of around  $\sqrt{0.3^2 + 0.4^2} = 50\%$  on the column densities. We note that the column densities measured from the spectra before (Table 6.1) and after subtraction of the emission lines agree within the uncertainties.

## 6.4.2 $\text{OCN}^-$

Here we are only interested in the  $\text{OCN}^-$  column densities to be used as a reference for column density ratios because of its potential chemical relation to  $\text{HNCO}$  (Schutte & Khanna 2003; Öberg et al. 2009a), another molecule observed abundantly in the gas-phase (e.g., Nazari et al. 2022a). Therefore, we report the column density of the red part of the  $\text{XCN}$  band (orange dashed line in Fig. 6.4) as the final  $\text{OCN}^-$  column density. From Fig. 6.4 it can be seen that  $\text{OCN}^-$  is detected in all sources and dominates the  $\text{XCN}$  band. We emphasize that this finding is unique to the spectra extracted from the apertures off-source as described in Sect. 6.2.1 (also see Fig. 6.A.1). The ice maps of  $\text{CO}$  and  $\text{OCN}^-$  found from this wavelength region are studied by Tyagi et al. (in preparation) for the IPA sources. Given the uncertainty on continuum identification of IRAS 16253, we do not analyze this object further. The band strength used for  $\text{OCN}^-$  to calculate the column density is taken from van Broekhuizen et al. (2004) as  $1.3 \times 10^{-16} \text{ cm per molecule}$ , and

the column densities are presented in Table 6.1. The uncertainties are estimated at the  $\sim 30\%$  level which is dominated by uncertainty on the band strength.

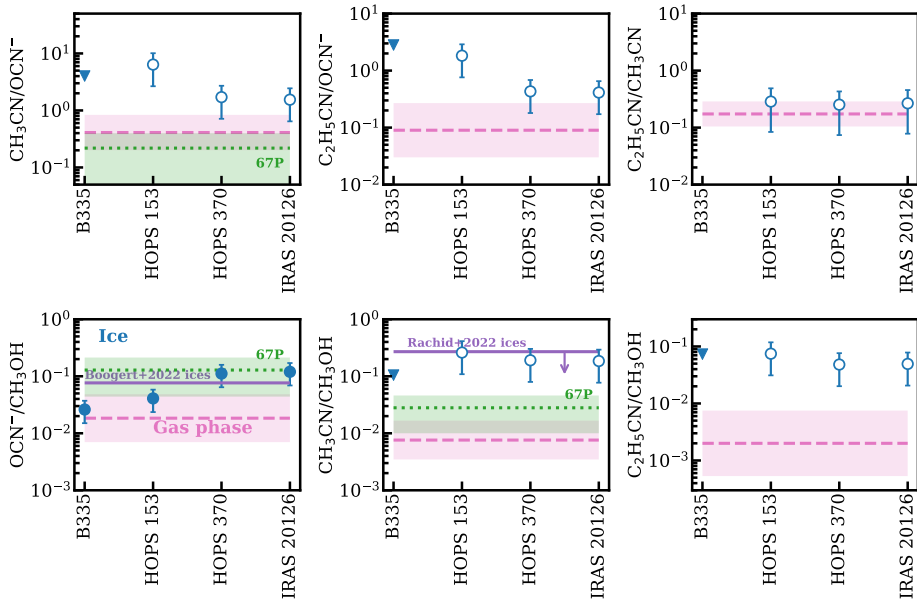
## 6.5 Ratios of icy cyanides and their comparison with gas-phase

Figure 6.5 presents the column density ratios of the considered species with respect to each other and their comparison with gas-phase observations. Our ice  $\text{OCN}^-/\text{CH}_3\text{OH}$  ratios (Fig. 6.5 bottom left) are consistent with the median of  $0.08^{+0.16}_{-0.07}$  found for 20 sources by Boogert et al. (2022). Moreover, our tentative column densities and upper limits for  $\text{CH}_3\text{CN}/\text{CH}_3\text{OH}$  (Fig. 6.5 bottom middle) agree well with the average upper limits of 0.27 found in ices for four protostellar systems by Rachid et al. (2022). An intriguing finding is that the column density ratio of  $\text{CH}_3\text{CN}/\text{OCN}^-$  in ices is around 1 (Fig. 6.5 top left). The main nitrogen ice carriers so far are thought to be  $\text{NH}_3$  and  $\text{NH}_4^+$  with a lesser contribution from  $\text{OCN}^-$  (e.g., Öberg et al. 2011; Boogert et al. 2015). Although not sufficient to solve the missing nitrogen problem (Pontoppidan et al. 2014; Altwegg et al. 2019), our results suggest that  $\text{CH}_3\text{CN}$  could be an important reservoir of nitrogen in the ices as well.

Comparing with comet 67P, our ice  $\text{OCN}^-/\text{CH}_3\text{OH}$  ratios agree within the uncertainties with  $\text{HNCO}/\text{CH}_3\text{OH}$  ratios in the comet (Fig. 6.5 bottom left). However, for  $\text{CH}_3\text{CN}/\text{OCN}^-$  (top left) and  $\text{CH}_3\text{CN}/\text{CH}_3\text{OH}$  (bottom middle) our ice ratios are a factor of  $\gtrsim 2$  larger than the comet values of  $\text{CH}_3\text{CN}/\text{HNCO}$  and  $\text{CH}_3\text{CN}/\text{CH}_3\text{OH}$ . Given the uncertainties, the significance of this difference is unclear.

Comparing with the gas-phase abundances, our ice ratios in the top row of Fig. 6.5 show a better agreement with gas-phase abundances than those in the bottom row. The tentative ice ratios of  $\text{C}_2\text{H}_5\text{CN}/\text{CH}_3\text{CN}$  (top right of Fig. 6.5) for our three sources are in particularly good agreement with the gas-phase observations at a ratio of  $\sim 0.1$ . This could highlight their similar origin and formation through connected chemical formation pathways. The ratios with respect to methanol (bottom row of Fig. 6.5),  $\text{OCN}^-/\text{CH}_3\text{OH}$ ,  $\text{CH}_3\text{CN}/\text{CH}_3\text{OH}$ , and  $\text{C}_2\text{H}_5\text{CN}/\text{CH}_3\text{OH}$ , show a large difference between the gas and ice (around a factor of 5 and up to a factor of  $\sim 20$ ).

These differences could be due to chemical effects, physical effects, or a combination of both. From a chemical perspective, given that the ratios with methanol seem to be most different, the chemistry of gas-phase methanol may require further study. For  $\text{OCN}^-/\text{CH}_3\text{OH}$ , we have assumed that all of  $\text{OCN}^-$  turns into  $\text{HNCO}$  (Öberg et al. 2009a), however, it is possible that not all the  $\text{OCN}^-$  in ices turns into gas-phase  $\text{HNCO}$ . For example, the efficiency of conversion of  $\text{OCN}^-$  to  $\text{HNCO}$  was not clear in the lab experiments of Jiménez-Escobar et al. (2014). Another possibility is that  $\text{OCN}^-$  could be trapped in ammonium salts as suggested to exist on comet 67P (Poch et al. 2020). Based on laboratory experiments those salts will then desorb at higher temperatures than methanol ( $\sim 200\text{ K}$  under laboratory conditions) and during the desorption these salts can decompose



**Figure 6.5:** Ice column density ratios (blue data points) of the species studied in this work with respect to each other and methanol taken from Slavicinska et al. (in preparation). Filled circles show firm detections, empty ones present the tentative column densities, and filled triangles show the upper limit values. The gas-phase column density ratios of many sources from the literature are shown in the pink shaded areas (the mean and standard deviation are taken from Nazari et al. 2022a). Here for the gas-phase observations we substitute  $\text{OCN}^-$  by  $\text{HNCO}$  because  $\text{OCN}^-$  is thought to turn into  $\text{HNCO}$  once sublimated. The purple lines show the previously measured ice column density ratios (median of values from Boogert et al. 2022) or upper limits (Rachid et al. 2022) in other sources. The abundance ratios of  $\text{CH}_3\text{CN}/\text{CH}_3\text{OH}$ ,  $\text{CH}_3\text{CN}/\text{HNCO}$ , and  $\text{HNCO}/\text{CH}_3\text{OH}$  for comet 67P are also shown in green (Rubin et al. 2019). See Fig. 6.A.4 for similar plots, but corrected for potential differences in emitting areas of the N-bearing species and methanol.

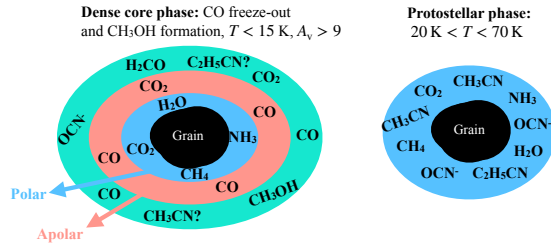
into HNCO and other species (Ligterink et al. 2018b). This difference in sublimation temperatures of  $\text{OCN}^-$  and  $\text{CH}_3\text{OH}$  can affect the column density ratios as explained further in the following paragraph.

In terms of physical effects, Nazari et al. (2021) showed that if two molecules have different sublimation temperatures (different snowline locations), the gas column density ratios will not represent the true ice abundance ratios (see their Sect. 4.3). This is because normally a single source size is assumed for all compact species when calculating the column densities in unresolved gas-phase protostellar observations (e.g., Jørgensen et al. 2018; Yang et al. 2021; van Gelder et al. 2022b). Therefore, a correction factor is needed to be multiplied by the gas-phase column density ratios which can be as large as a factor of  $\sim 10$  if the two molecules in the ratio have sufficiently different sublimation temperatures (e.g.,  $\text{CH}_3\text{OH}$ ,  $\sim 100$  K, and  $\text{NH}_2\text{CHO}$ ,  $\sim 300$  K, also see Fig. 5 in Nazari et al. 2023b). The binding energies and sublimation temperatures of  $\text{CH}_3\text{CN}$ ,  $\text{C}_2\text{H}_5\text{CN}$ , and  $\text{CH}_3\text{OH}$  in the amorphous water ice matrix are similar ( $T_{\text{sub}} \sim 100$  K; Penteado et al. 2017; Minissale et al. 2022; Ligterink & Minissale 2023), so the correction factor is negligible. However, if these molecules are part of a different ice matrix the binding energies change. Thus a more direct measurement of the temperature that they trace is based on the excitation temperatures ( $T_{\text{ex}}$ ) of the gas phase observations. The  $T_{\text{ex}}$  for the bulk of gas-phase observations in Fig. 6.5 (pink shaded area) for  $\text{CH}_3\text{CN}$  and HNCO is around 150 K while for methanol it is around 100 K (Fig. 6 of Nazari et al. 2022a). Hence the correction factor to be applied to the gas-phase observations with respect to methanol is expected to be  $(150/100)^{3.75} = 4.6$  based on a spherical toy model (see Eq. 4 in Nazari et al. 2021).

Including a correction factor of 4.6 in the gas-phase abundances of the bottom row (see Fig. 6.A.4) results in the gas-phase observations of  $\text{OCN}^-/\text{CH}_3\text{OH}$  matching the ice observations within a factor of a few. Moreover, the gas-phase observations of  $\text{CH}_3\text{CN}/\text{CH}_3\text{OH}$  and  $\text{OCN}^-/\text{CH}_3\text{OH}$ , which previously did not match the comet 67P ratios of  $\text{CH}_3\text{CN}/\text{CH}_3\text{OH}$  and HNCO/ $\text{CH}_3\text{OH}$ , now match the comet ratios (Rubin et al. 2019). Considering the uncertainties and the small sample size it is not possible to argue whether there is still a difference between the gas and ice observations of  $\text{CH}_3\text{CN}$  and  $\text{C}_2\text{H}_5\text{CN}$  ratios with respect to methanol. We conclude that when the physical effects are considered, the ice- and gas-phase observations are in much closer agreement with each other.

Finally, to confirm the detection and column density measurements of this work (i.e., detection of at least two ice bands for each molecule), both NIRSpect and MIRI data of these sources should be analyzed in the future. Figure 6.A.5 presents the laboratory spectrum of pure  $\text{CH}_3\text{CN}$  and  $\text{C}_2\text{H}_5\text{CN}$  in the  $2.5 - 12.5 \mu\text{m}$  regime. We note the  $\text{CH}_3\text{CN}$  feature at  $3.33 \mu\text{m}$ , which has a smaller band strength than the feature analyzed here, falls in the bulk stretch of the  $\text{H}_2\text{O}$  ice band and thus is challenging to detect. After the strongest feature at  $4.44 \mu\text{m}$ , the next best features are in the wavelength range of MIRI ( $\sim 6.8 - 7.4 \mu\text{m}$ ). Those are particularly promising because of their larger FWHM and thus their larger or similar band strengths (Rachid et al. 2022). Although those features are embedded in strong ice features of other simple and complex species (Yang et al. 2022; Rocha et al. 2023), they could provide an additional constraint on the column densities

**Figure 6.6:** Sketch of typical dust grain chemical inventory. We suggest that  $\text{OCN}^-$ ,  $\text{CH}_3\text{CN}$  and  $\text{C}_2\text{H}_5\text{CN}$  likely start to form in the cold dense core phase but are enhanced thermally during the warm-up stage where more volatile species have sublimated.



of complex cyanides.

## 6.6 Chemical interpretation

### 6.6.1 Origin of complex cyanides

$\text{OCN}^-$  is thought to start forming in the dense core phase after the CO freeze-out (see the review by Boogert et al. 2015). Because the  $\text{CH}_3\text{CN}:\text{CO}$  mixture was needed to fit the data, we speculate that  $\text{CH}_3\text{CN}$  starts forming in this same phase along with  $\text{OCN}^-$  (Fig. 6.6). In fact, this agrees with the constant gas-phase column density ratios of  $\text{CH}_3\text{CN}/\text{CH}_3\text{OH}$  with some low-level scatter found for a large sample of protostars by Nazari et al. (2022a), which points to their formation likely in the cold prestellar phase. This interpretation also agrees with our finding that gas and ice ratios are similar to each other after correction for source structure. The other important ice mixture explaining the data is  $\text{CH}_3\text{CN}:\text{H}_2\text{O}:\text{CO}_2$ , which is expected if the ices are thermally processed (see Sect. 6.6.2). We emphasize that the spectral fits presented here (Fig. 6.3) are not unique, however, mixtures of  $\text{CH}_3\text{CN}$  with CO or  $\text{NH}_3$ ,  $\text{CO}_2$  and  $\text{H}_2\text{O}$  are always needed. Because there are no laboratory spectra of  $\text{C}_2\text{H}_5\text{CN}$  ice mixtures, we cannot constrain its ice environment. The simplest assumption is that it also starts forming with  $\text{OCN}^-$  and  $\text{CH}_3\text{CN}$  in the dense core phase.

### 6.6.2 Thermal processing

Clues on the formation pathways are obtained by considering the relation between column density ratios and the bolometric luminosity. The  $\text{OCN}^-/\text{CH}_3\text{OH}$  ratios increase slightly with luminosity for our sample (Fig. 6.7). Additional sources are needed to confirm this relation. The  $\text{OCN}^-$  ice feature is enhanced at higher temperatures in laboratory experiments (e.g., Novozamsky et al. 2001; van Broekhuizen et al. 2004), and a potential correlation between  $\text{OCN}^-$  and luminosity is justified if the sources with higher luminosities also have higher ice temperatures with more volatile species sublimated. Brunken et al. (submitted) use spectra extracted on-source and find that IPA sources with higher bolometric luminosities also show a more prominent  $^{13}\text{CO}_2$  double-peaked ice feature, which is known to indicate ice thermal processing. The locations where we extracted the spectra still show a prominent  $^{13}\text{CO}_2$  double-peaked feature for IRAS 20126

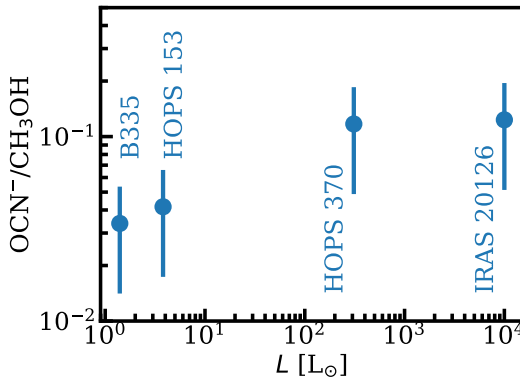


**Figure 6.7:** Column density ratios of  $\text{OCN}^-/\text{CH}_3\text{OH}$  as a function of luminosity for the IPA sources.

and HOPS 370 (Fig. 6.1), while the double-peaked feature is less prominent (or non-existent) for the other sources. Therefore, ices of IRAS 20126 and HOPS 370 (the two most luminous sources in the sample) are warmer than the other sources and thus,  $\text{OCN}^-$  formation is likely enhanced (Fig. 6.6).

It is interesting to note that the three sources with a tentative detection of  $\text{CH}_3\text{CN}$  and  $\text{C}_2\text{H}_5\text{CN}$  are those with the highest luminosities and potentially warmest ices. Moreover, the laboratory  $\text{CH}_3\text{CN}:\text{CO}$  ice mixture that fitted the data best were those at high temperatures. Hence formation of  $\text{CH}_3\text{CN}$  and  $\text{C}_2\text{H}_5\text{CN}$  might be enhanced in warmer ices. However, the non-detection in the other two sources could be simply a sensitivity problem. Therefore, a larger sample size in which these ices are detected with a range in luminosities and masses is needed to further study thermal processing of  $\text{CH}_3\text{CN}$  and  $\text{C}_2\text{H}_5\text{CN}$  in interstellar ices.

Nevertheless, this potential enhancement of  $\text{CH}_3\text{CN}$  and  $\text{C}_2\text{H}_5\text{CN}$  formation at higher temperatures is expected from their ice formation pathways. In the ice,  $\text{CH}_3\text{CN}$  is thought to form through reaction of two radicals  $\text{CH}_3$  and  $\text{CN}$  (Garrod et al. 2008; Garrod et al. 2022). Because ice radicals can have higher mobility at higher temperatures,  $\text{CH}_3\text{CN}$  production can increase. For  $\text{C}_2\text{H}_5\text{CN}$ , laboratory experiments using UV photolysis (Bulak et al. 2021) found that higher temperatures enhance the formation of  $\text{C}_2\text{H}_5\text{CN}$  from  $\text{CH}_3\text{CN}$ -based ices. Enhanced formation of  $\text{CH}_3\text{CN}$  and  $\text{C}_2\text{H}_5\text{CN}$  in warmer ices can also help explain the low-level scatter in the column density ratios of gas-phase observations (pink area in Fig. 6.5).

## 6.7 Conclusions

In this paper we report the first tentative detection of  $\text{CH}_3\text{CN}$ ,  $\text{C}_2\text{H}_5\text{CN}$ , and  $\text{N}_2\text{O}$  in ices around three embedded protostars (HOPS 153, HOPS 370, and IRAS 20126+4104). Our  $\text{CH}_3\text{CN}/\text{OCN}^-$  ice ratios are on the order of 1, suggesting that  $\text{CH}_3\text{CN}$  could be a significant nitrogen reservoir in ices. Our ice column density

ratios among the nitrogen-bearing species agree better between the gas and ice observations in comparison to those with respect to methanol which are around a factor of 5 larger in ices than the gas-phase. We attribute this to the difference in the snowline locations of  $\text{CH}_3\text{OH}$  and the nitrogen-bearing species studied here.

The main ice mixtures that fit the data are those where  $\text{CH}_3\text{CN}$  is mixed with  $\text{H}_2\text{O}$ ,  $\text{CO}_2$  and  $\text{CO}$ . We conclude that  $\text{CH}_3\text{CN}$  and  $\text{C}_2\text{H}_5\text{CN}$  likely start forming in the dense core phase after the  $\text{CO}$  freeze-out and could be further enhanced during the warm-up stage around the protostar.

*JWST*-NIRSpec data presented here help in understanding the chemistry and formation mechanism of complex cyanides. However a much larger sample of protostars with both NIRSpec and MIRI data are needed to firmly identify and statistically measure the significance of the relations proposed here.

### Acknowledgments

We thank the referee for their constructive comments. P.N. greatly appreciates the helpful discussions with Danial Langeroodi. Astrochemistry in Leiden is supported by the Netherlands Research School for Astronomy (NOVA), by funding from the European Research Council (ERC) under the European Union’s Horizon 2020 research and innovation programme (grant agreement No. 101019751 MOLDISK), and by the Dutch Research Council (NWO) grant 618.000.001. Support by the Danish National Research Foundation through the Center of Excellence “Inter-Cat” (Grant agreement no.: DNRF150) is also acknowledged. Support for AER, STM, RG, DW, and SF in program #1802 was provided by NASA through a grant from the Space Telescope Science Institute, which is operated by the Association of Universities for Research in Astronomy, Inc., under NASA contract NAS 5-03127. G.A. and M.O. acknowledge financial support from grants PID2020-114461GB-I00 and CEX2021-001131-S, funded by MCIN/AEI/10.13039/501100011033. Y.-L.Y. acknowledges support from Grant-in-Aid from the Ministry of Education, Culture, Sports, Science, and Technology of Japan (20H05845, 20H05844, 22K20389), and a pioneering project in RIKEN (Evolution of Matter in the Universe). This work is based on the observations with the NASA/ESA/CSA James Webb Space Telescope. The data were obtained from the Mikulski Archive for Space Telescopes at the Space Telescope Science Institute, which is operated by the Association of Universities for Research in Astronomy, Inc., under NASA contract NAS 5-03127 for *JWST*. These observations are associated with program #1802. All the *JWST* data used in this paper can be found in MAST: 10.17909/3kky-t040.

## Appendix

### 6.A Additional tables and plots

Table 6.A.1 presents the centers of the apertures from which the spectra are extracted, in addition to the rms on the continuum optical depth and the source characteristics. Table 6.A.2 presents the band strengths used for the column density measurements. Figure 6.A.1 illustrates the positions from which the spectra

**Table 6.A.1:** Positions for spectral extraction and source properties

Source	R.A. [hh:mm:ss]	Decl. [dd:mm:ss]	Optical depth rms	$L_{\text{bol}}$ [ $L_{\odot}$ ]	$d$ [pc]	References
IRAS 16253	16:28:21.71	-24:36:23.06	0.0045	0.16	140	Ortiz-León et al. (2018b); Aso et al. (2023)
B335	19:37:01.03	07:34:07.70	0.014	1.4	165	Watson (2020); Evans et al. (2023)
HOPS 153	05:37:57.11	-07:06:57.30	0.0076	3.8	390	Tobin et al. (2020)
HOPS 370	05:35:27.50	-05:09:32.65	0.0009	315.7	390	Tobin et al. (2020)
IRAS 20126	20:14:26.10	41:13:29.46	0.0026	$10^4$	1550	Johnston et al. (2011); Reid et al. (2019)

**Notes.** Second and third column give the right ascension and declination of the center of the aperture used to extract the spectrum (see Fig. 6.A.1). The references of bolometric luminosities and distances of the central sources are given in the right-most column.

are extracted in this work. Figure 6.A.2 presents the local continuum fits to the extracted spectra. Figure 6.A.3 presents the fit to the CN-stretching region for the emission-line-subtracted spectra (see Rubinstein et al. 2023). Figure 6.A.4 is the same as Fig. 6.5 but for corrected gas-phase column density ratios. Figure 6.A.5 presents the laboratory spectra of pure  $\text{CH}_3\text{CN}$  and  $\text{C}_2\text{H}_5\text{CN}$  to highlight the strongest features.

**Table 6.A.2:** Band strengths

Ice species	$A$ ( $\text{cm molecule}^{-1}$ )
$\text{CH}_3\text{CN}:\text{CO}_2$	$1.5 \times 10^{-18}$
$\text{CH}_3\text{CN}:\text{CO}$	$1.5 \times 10^{-18}$
$\text{CH}_3\text{CN}:\text{H}_2\text{O}:\text{CO}_2$	$3.3 \times 10^{-18}$
$\text{C}_2\text{H}_5\text{CN}$	$2.9 \times 10^{-18}$
$\text{OCN}^-$	$1.3 \times 10^{-16}$

**Notes.** The band strengths are taken from Rachid et al. (2022) and van Broekhuizen et al. (2004) for  $\text{CH}_3\text{CN}$  mixtures and  $\text{OCN}^-$ , respectively, while they are calculated for  $\text{C}_2\text{H}_5\text{CN}$  in this work.

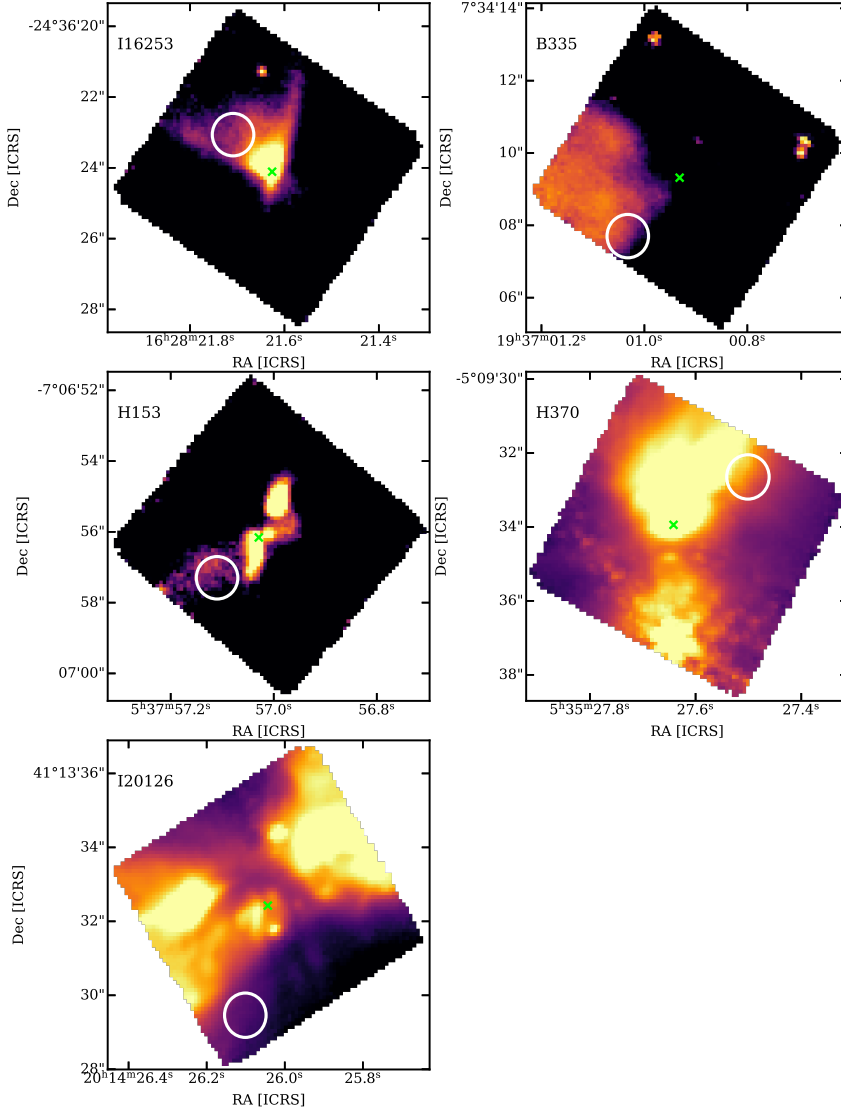


**Figure 6.A.1:** *JWST*-NIRSpec continuum images at  $3.92 \mu\text{m}$  for the IPA targets. White circles show the apertures from which the spectra are extracted in this work to avoid the CO rotational-vibrational emission lines as much as possible. The central position of each protostar according to the IPA-MIRI channel 3 medium band is shown by a green cross.

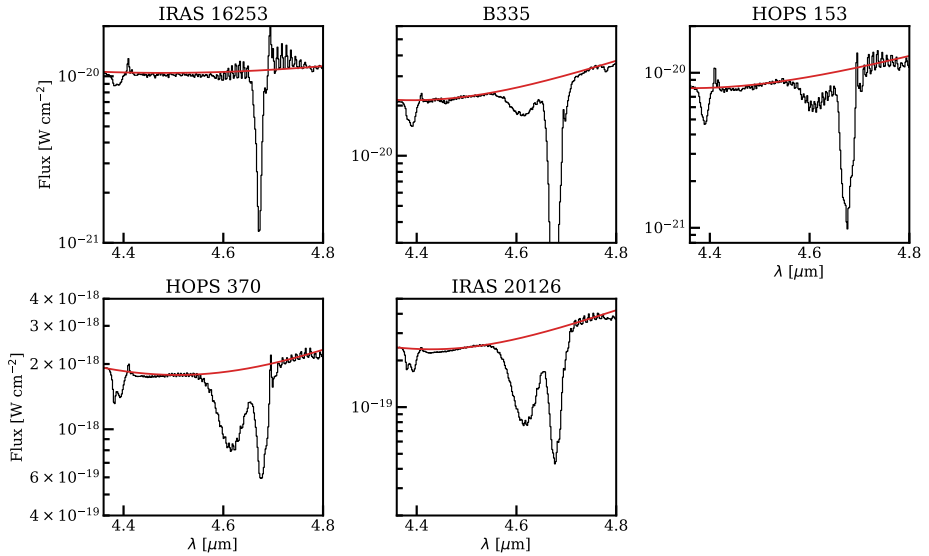


**Figure 6.A.2:** Spectra (black) and the fitted continuum (red) for all the five sources in the IPA program. The continuum is fitted locally using a polynomial function.

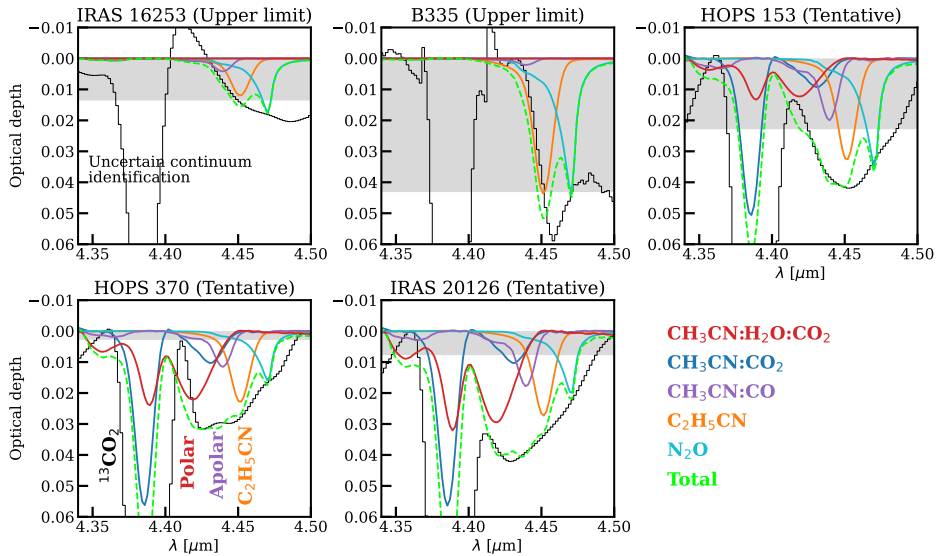


**Figure 6.A.3:** Same as Fig. 6.3 but for the emission-line-subtracted spectra taken from Rubinstein et al. (2023) where the methods of emission line fitting and subtraction are explained.

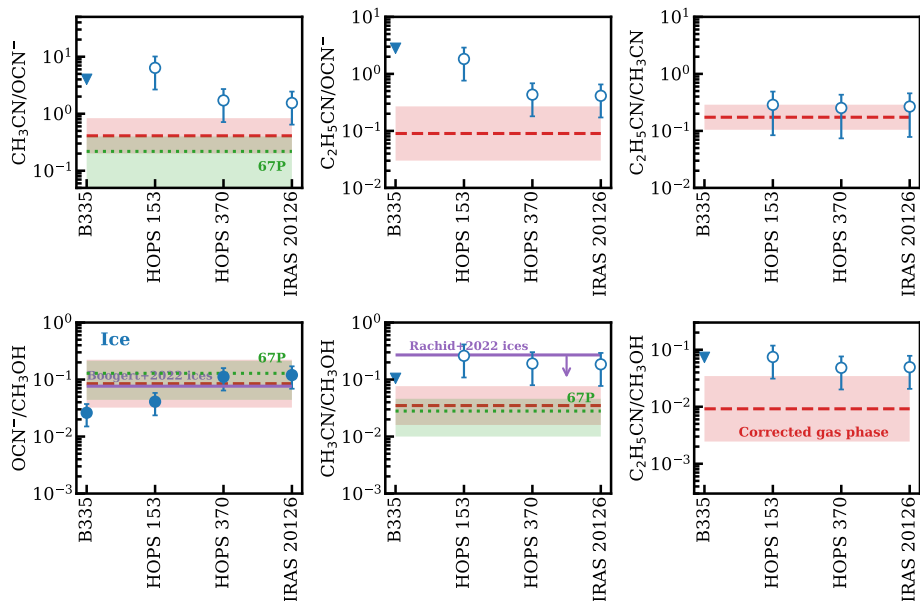


**Figure 6.A.4:** Same as Fig. 6.5 but now the gas-phase column density ratios are corrected by a factor of 4.6 for potential differences between the snowline locations of nitrogen-bearing molecules with respect to methanol.

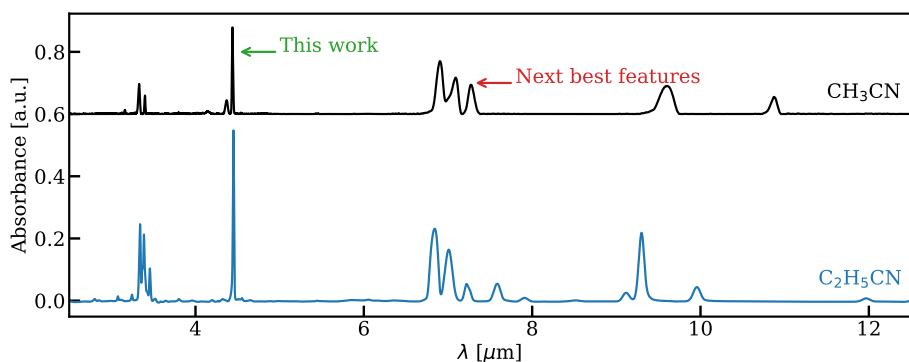


**Figure 6.A.5:** Laboratory spectra of pure  $\text{CH}_3\text{CN}$  and  $\text{C}_2\text{H}_5\text{CN}$  at 15 K and 50 K, respectively, to highlight which feature can be used in the future for firm detection of these two species. The spectrum of  $\text{CH}_3\text{CN}$  is shifted vertically for better readability.